Electronic Supplementary Material (ESI) for Journal of Materials Chemistry A.

Supporting Information

Controllable growth of SnS_2 nanostructures on nanocarbon surfaces for Lithium-ion and Sodium-ion storage with high rate capability

Bin Luo,[a] Yuxiang Hu,[a] Xiaobo Zhu,[a] Tengfei Qiu,[b] Linjie Zhi,[b]* Mu Xiao,[a] Haijiao Zhang,[c]* Mingchu Zou,[d] Anyuan Cao,[d] and Lianzhou Wang[a]*

[a] Nanomaterials Centre, School of Chemical Engineering and Australian Institute for Bioengineering and Nanotechnology, The University of Queensland. St Lucia QLD 4072, Australia. E-mail: l.wang@uq.edu.au

[b] National Centre for Nanoscience and Technology, China. Zhongguancun, Beiyitiao No. 11 Beijing, 100190, P. R. China. E-mail: zhilj@nanoctr.cn

[c] Institute of Nanochemistry and Nanobiology, Shanghai University, Shanghai 200444, China. E-mail: hjzhang128@shu.edu.cn

[d] Department of Materials Science and Engineering, College of Engineering, Peking University. Beijing 100871, P. R. China

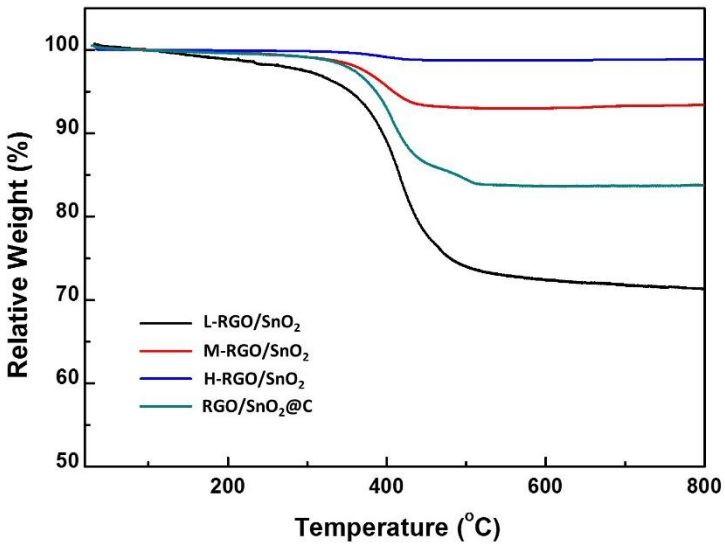

Fig. S1. TGA of the RGO/SnO_2 based composite precursors with different SnO_2 mass loading on RGO. The measurements were taken in air using a heating rate of 10℃ min^{-1}.

SnO_2 contents of L-RGO/SnO_2, M-RGO/SnO_2, H-RGO/SnO_2 and RGO/SnO_2@C estimated from the thermal analysis are ca. 71.3, 93.4, 97.4 and 83.7 wt %, respectively. The corresponding SnS_2 contents of these samples after sulfuration were also estimated based on the following equation S1 as all SnO_2 would be converted into SnS_2 during the sulfuration process (equation S2), as shown in Table S1.

$$C_{SnS_2}(wt\%) = \frac{m_{SnS_2}}{m_{\text{Carbon}} + m_{SnS_2}} = 100\% \times \frac{(M_{SnS_2} / M_{SnO_2}) \times m_{SnO_2}}{(m_{Carbon/SnO_2} - m_{SnO_2}) + (M_{SnS_2} / M_{SnO_2}) \times m_{SnO_2}} \quad \text{(S1)}$$

$$SnO_2 + 2H_2S \rightarrow SnS_2 + 2H_2O \quad \text{(S2)}$$

Table S1. SnO_2 contents and the corresponding SnS_2 contents of these samples after sulfuration of L-RGO/SnO_2, M-RGO/SnO_2, H-RGO/SnO_2 and RGO/SnO_2@C.

	SnO_2 content	Estimated SnS_2 content after sulfuration
L-RGO/SnO_2	71.3	75.1
M-RGO/SnO_2	93.4	94.4
H-RGO/SnO_2	97.4	97.8
RGO/SnO_2@C	83.7	86.2

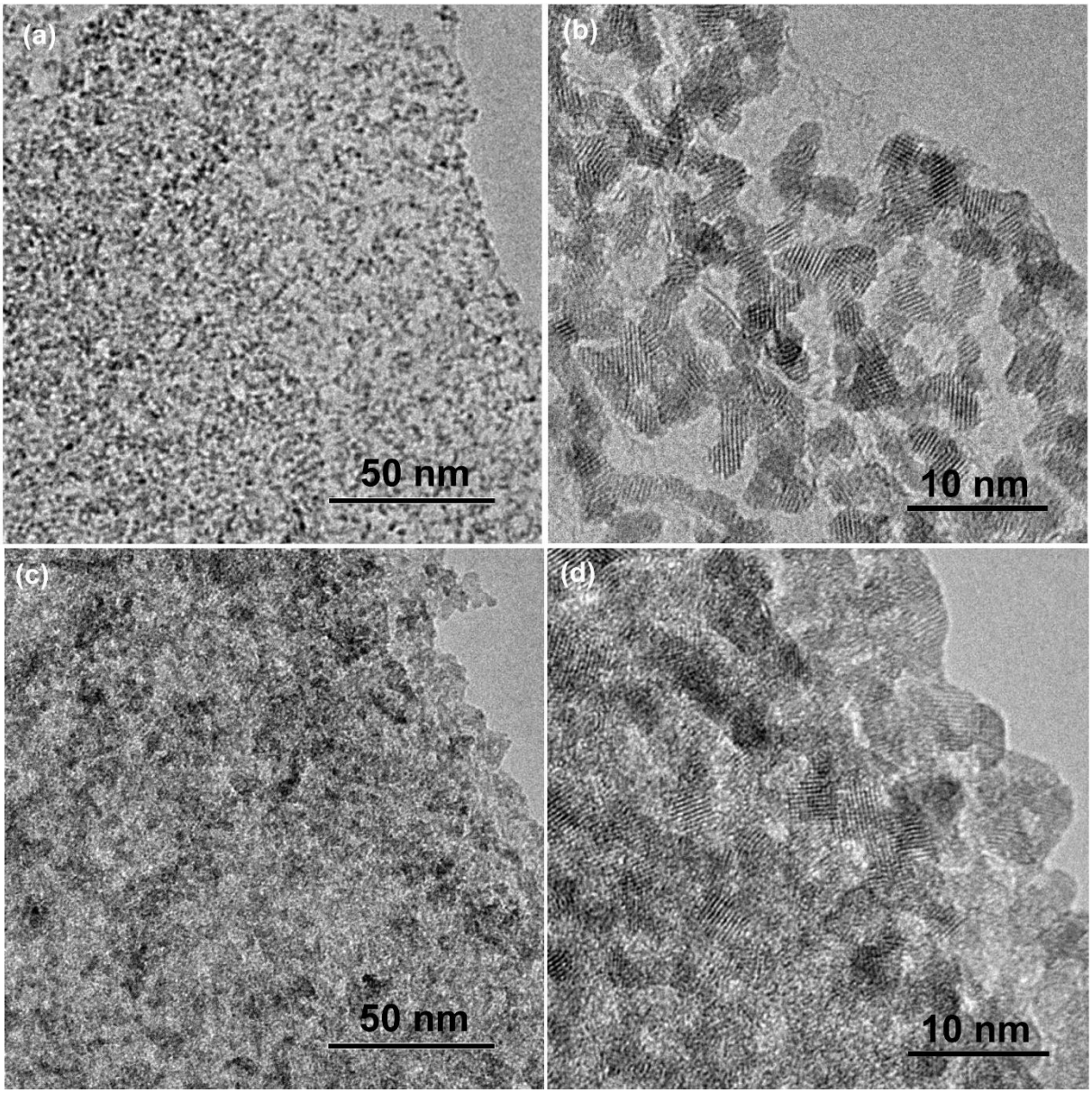

Fig. S2. TEM and HRTEM images of (a, b) the low SnO_2 mass loaded precursor (L-RGO/SnO_2) and (c, d) the high SnO_2 mass loaded precursor (H-RGO/SnO_2).

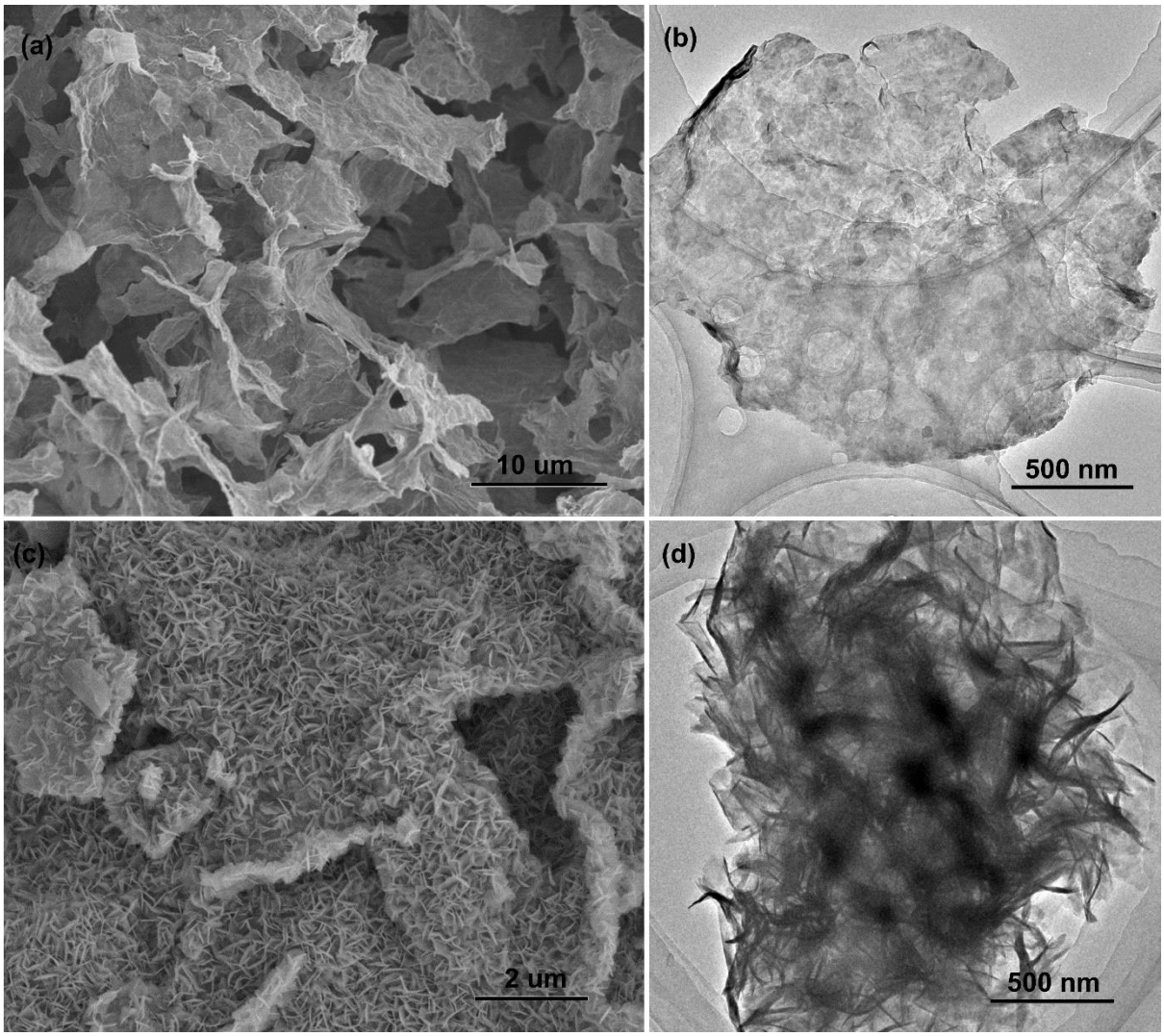

Fig. S3. Low magnification SEM and TEM images of (a ,b) P-RGO/SnS_2 and (c, d) V-RGO/SnS_2 composites.

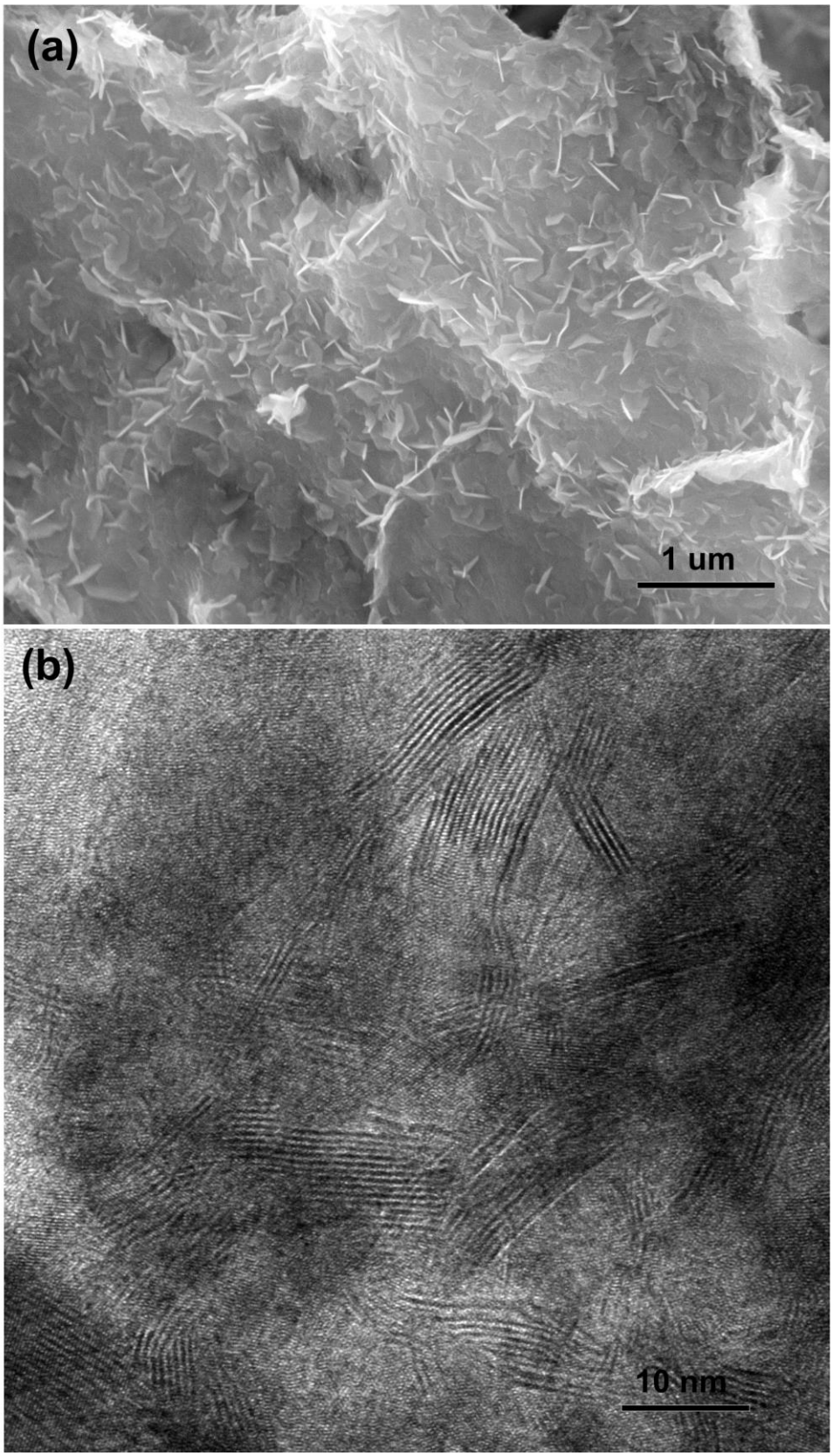

Fig. S4 SEM and TEM images of the RGO/SnS_2 composite obtained from the medium SnO_2 mass loaded RGO/SnO_2 precursor (M-RGO/SnO_2).

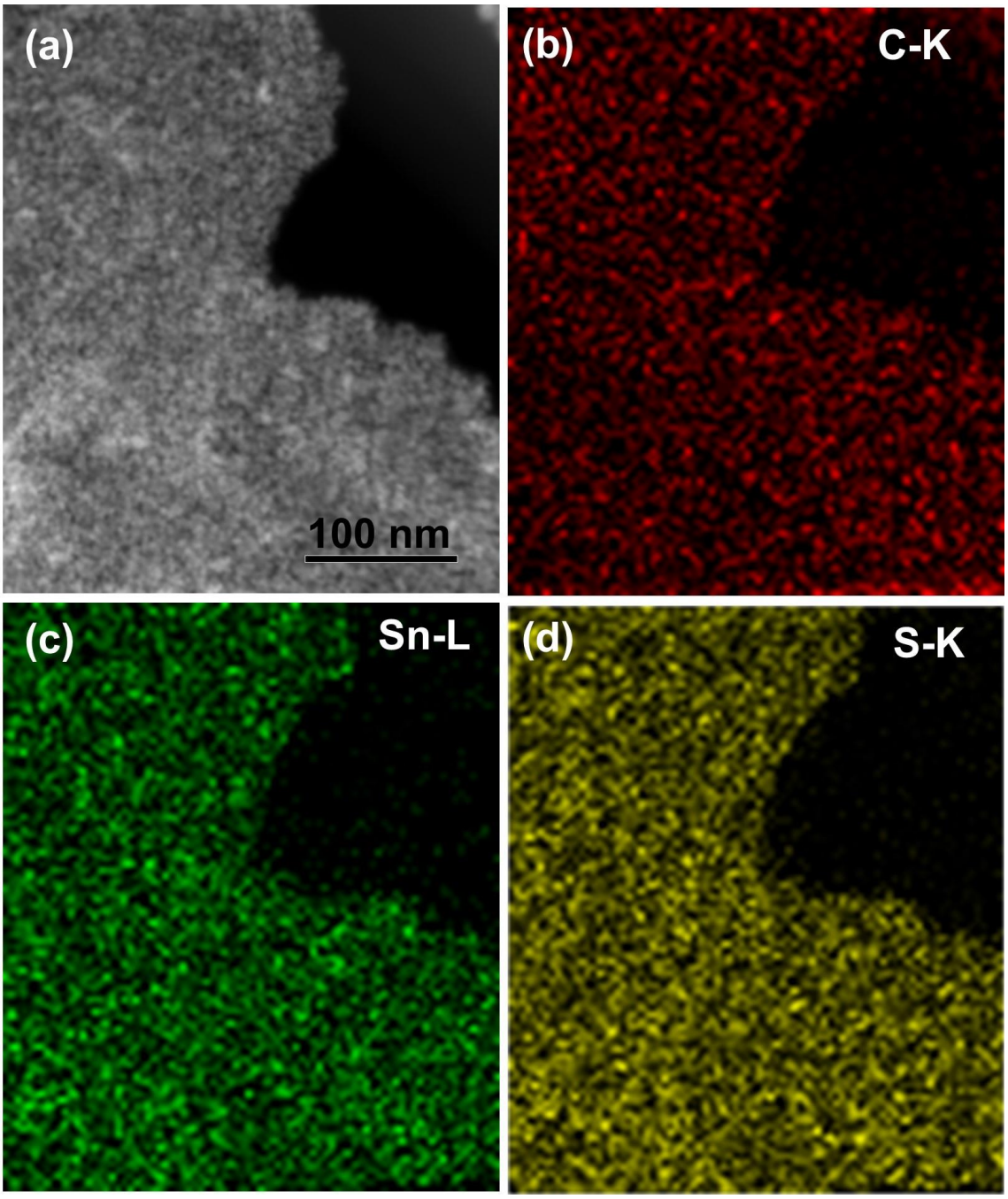

Fig. S5. (a) STEM image, and (b-d) Element mapping images of the RGO/SnS_2@C composite, showing the uniform distribution of SnS_2 nanoparticles within the RGO backboned 2D carbon matrix.

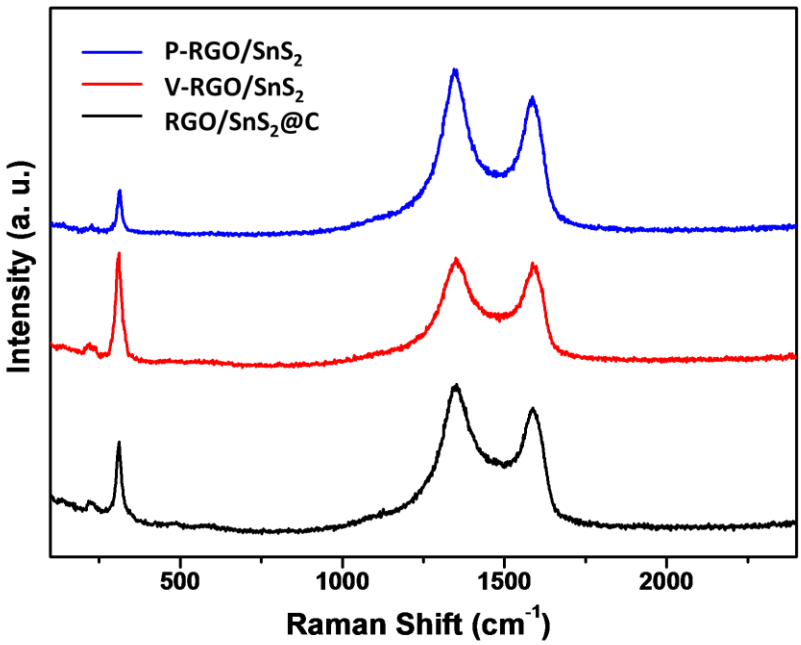

Fig. S6 Raman spectra of P-RGO/SnS_2, V-RGO/SnS_2 and RGO/SnS_2@C composites. All the Raman spectra exhibit an intense peak at about 311 cm^{-1}, which is attributed to the A_{1g} mode of SnS_2. The peak at about 1585 cm^{-1}(G band) is related to the vibration of the sp^2-bonded carbon atoms in a 2-dimensional hexagonal lattice, while the peak at about 1325 cm^{-1} (D band) is related to the defects and disorder in the hexagonal graphitic layers.

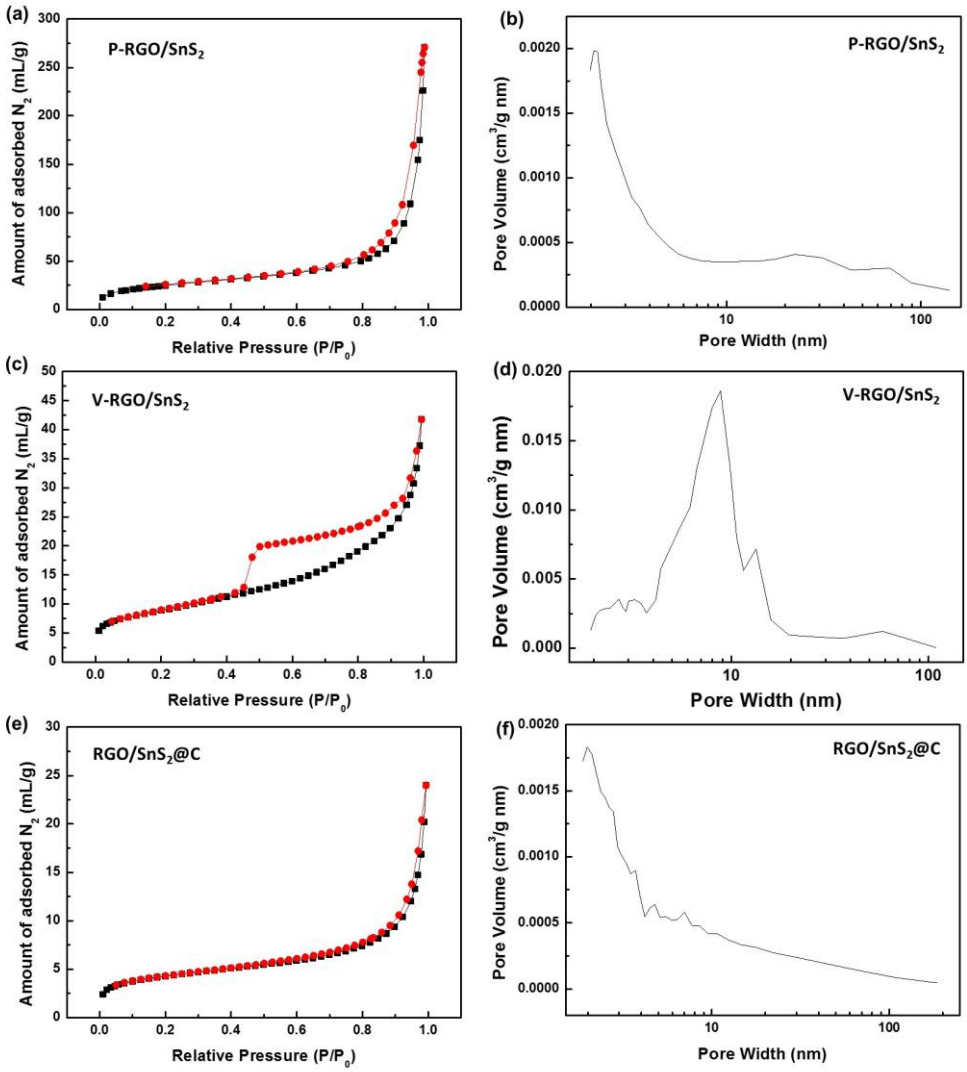

Figure S7. Nitrogen adsorption-desorption isotherms and pore-size distribution of (a, b) P-RGO/SnS_2, (c, d) V-RGO/SnS_2 and (e, f) RGO/SnS_2@C composites, respectively.

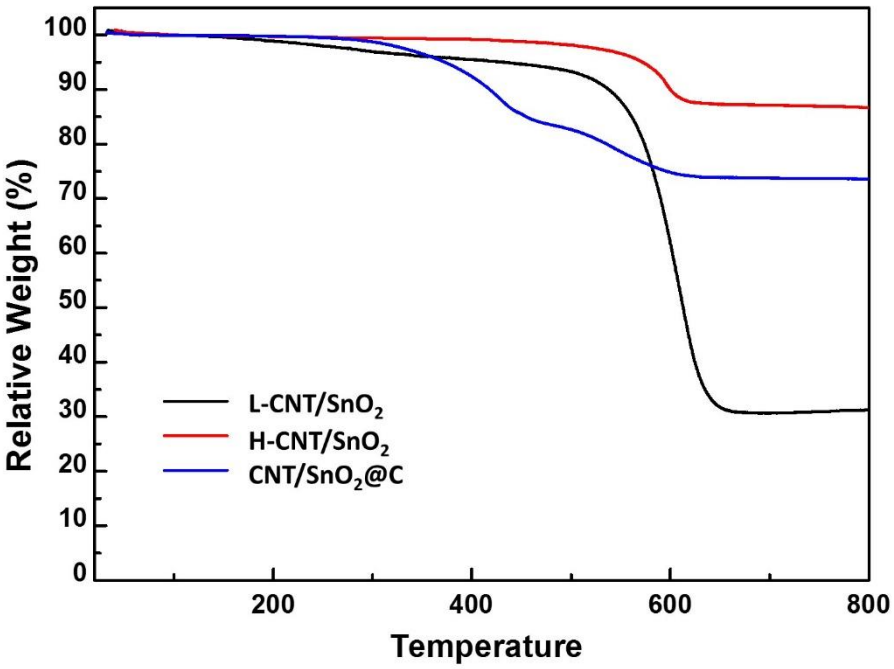

Fig. S8. TGA of the RGO/SnO_2 based composite precursors with different SnO_2 mass loading on RGO. The measurements were taken in air using a heating rate of 10℃ min^{-1}.

SnO_2 contents of L-CNT/SnO_2, H-CNT/SnO_2 and CNT/SnO_2@C estimated from the thermal analysis are ca. 31.2, 86.7 and 73.6 wt %, respectively. The corresponding SnS_2 contents of these samples after sulfuration were also estimated based on the following equation S1 as all SnO_2 would be converted into SnS_2 during the sulfuration process (equation S2), as shown in Table S2.

Table S2. SnO_2 contents and the corresponding SnS_2 contents of these samples after sulfuration of L-CNT/SnO_2, H-CNT/SnO_2 and CNT/SnO_2@C.

	SnO_2 content	Estimated SnS_2 content after sulfuration
L-CNT/SnO_2	31.2	35.3
H-CNT/SnO_2	86.7	88.7
CNT/SnO_2@C	73.6	77.1

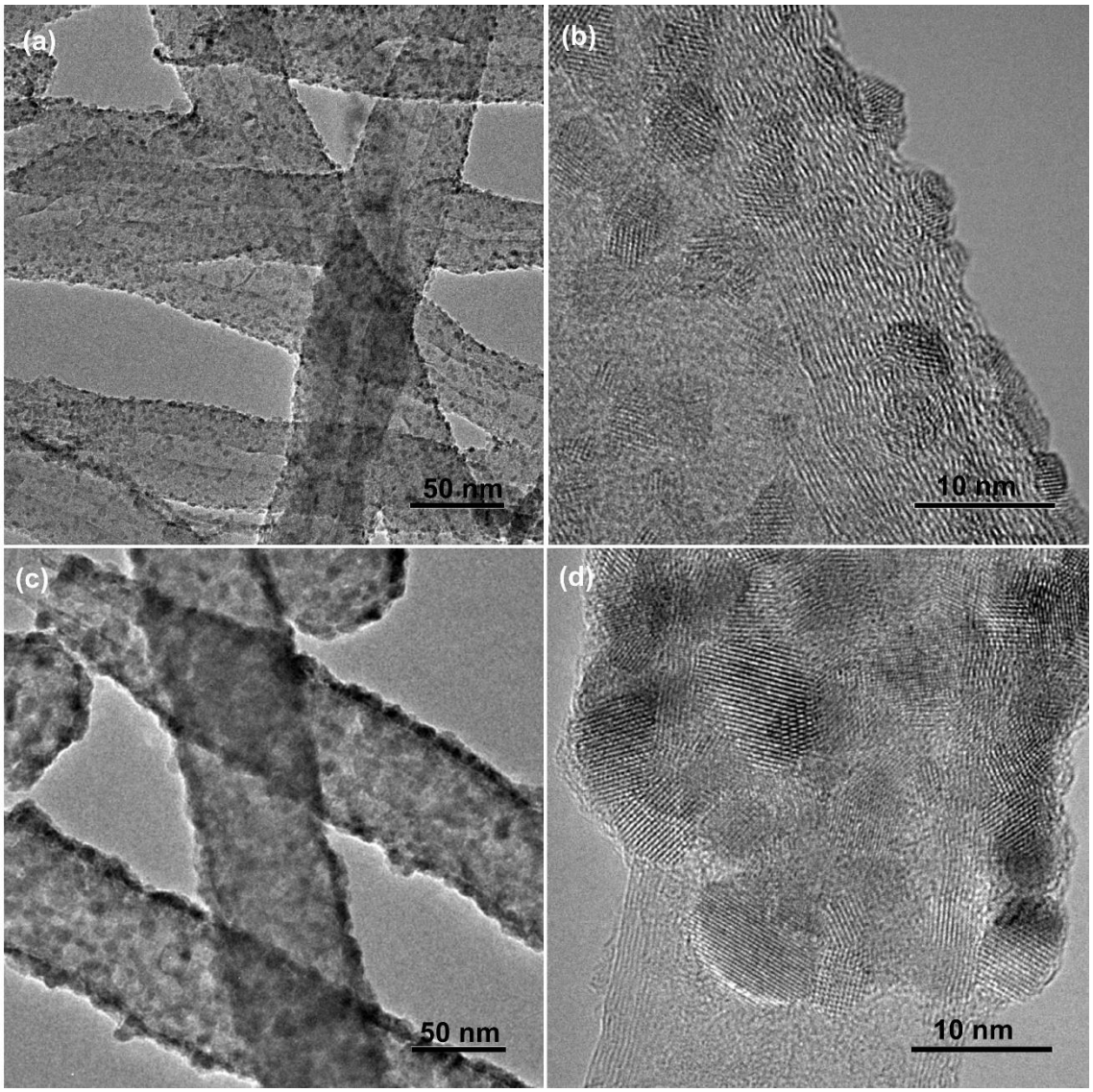

Fig. S9. TEM and HRTEM images of (a, b) the low SnO_2 mass loaded CNT/SnO_2 precursor (L-CNT/SnO_2) and (c, d) the high SnO_2 mass loaded CNT/SnO_2 precursor (H-CNT/SnO_2).

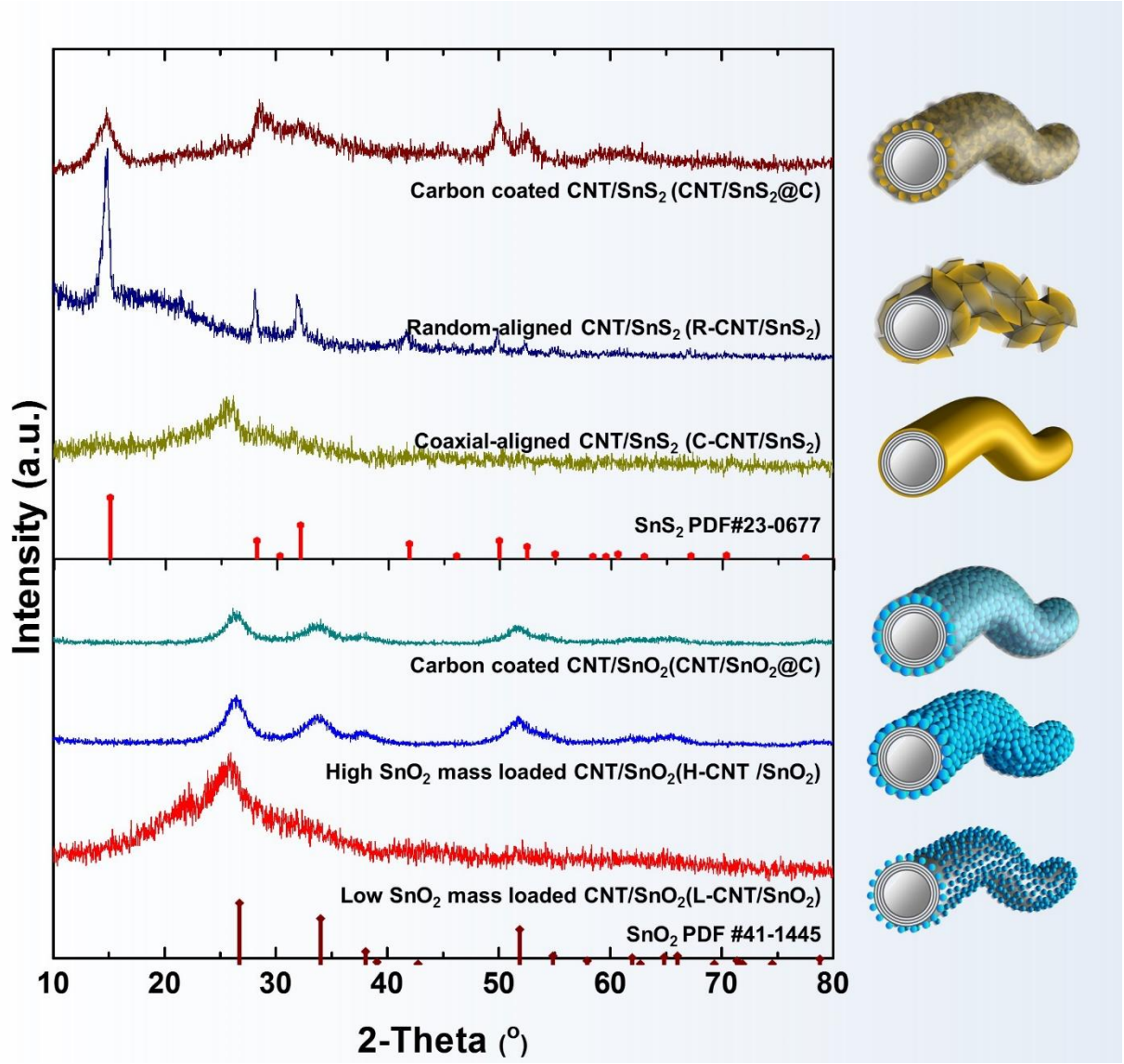

Fig. S10. X-ray diffraction patterns of the CNT based composites, including the L-CNT/SnO_2, H-CNT/SnO_2 and CNT/SnO_2@C precursors and the corresponding products after sulfuration, C-CNT/SnS_2, R-CNT/SnS_2 and CNT/SnS_2@C.

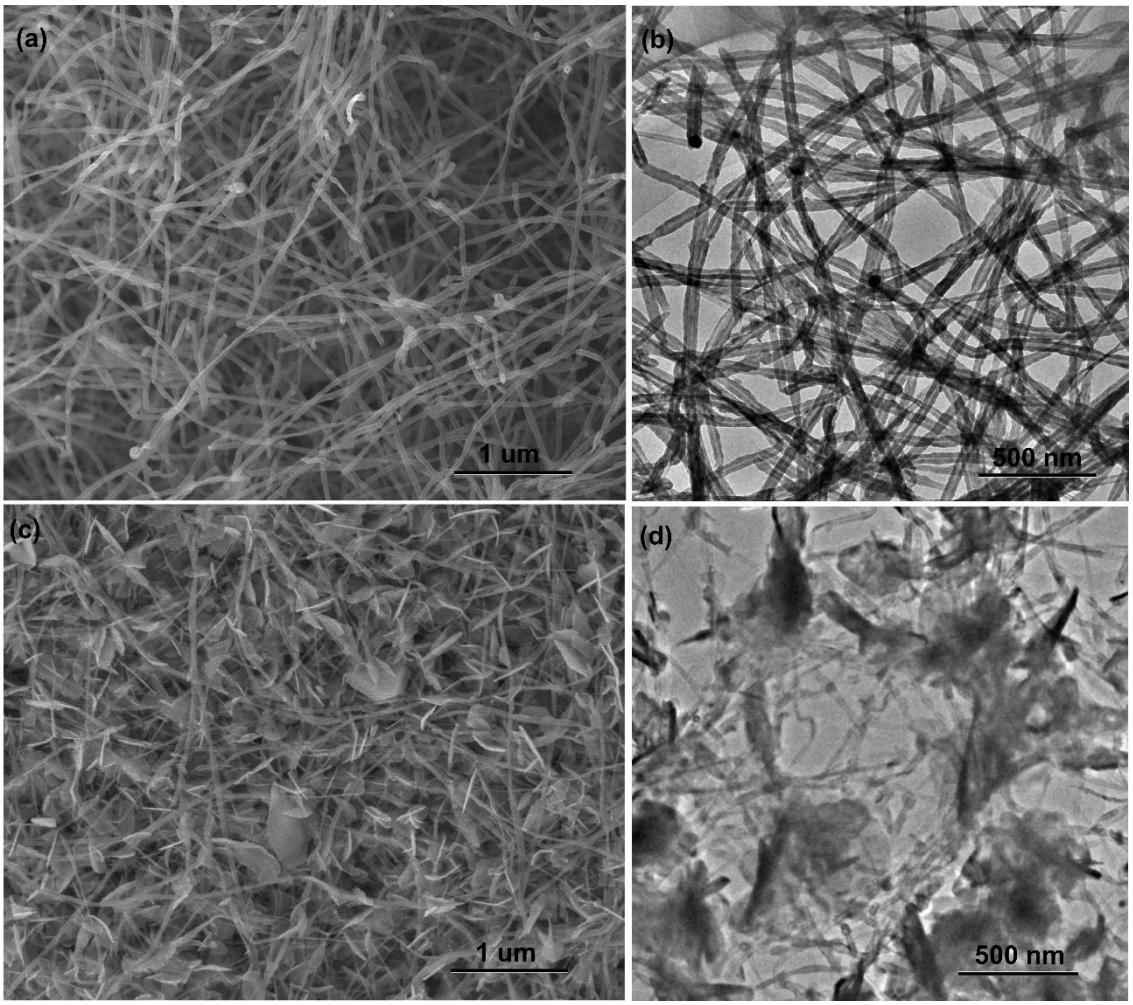

Fig. S11. Low magnification SEM and TEM images of (a ,b) C-CNT/SnS_2 and (c, d) R-CNT/SnS_2 composites.

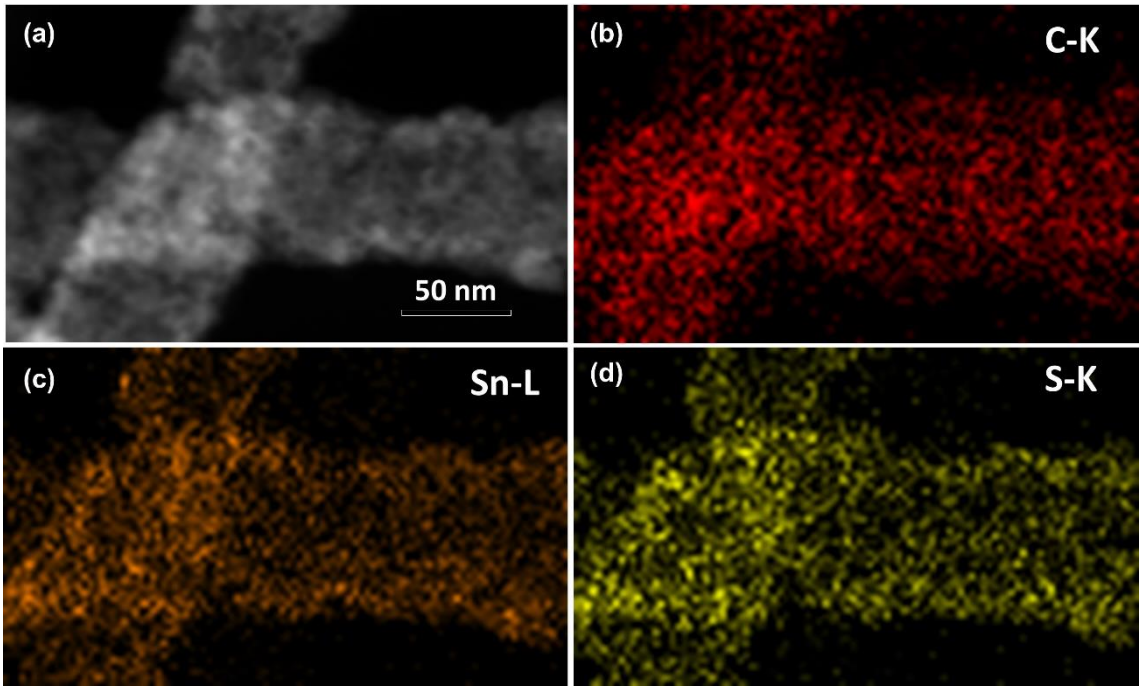

Fig. S12. (a) STEM image, and (b-d) Element mapping images of the CNT/SnS_2@C composite.

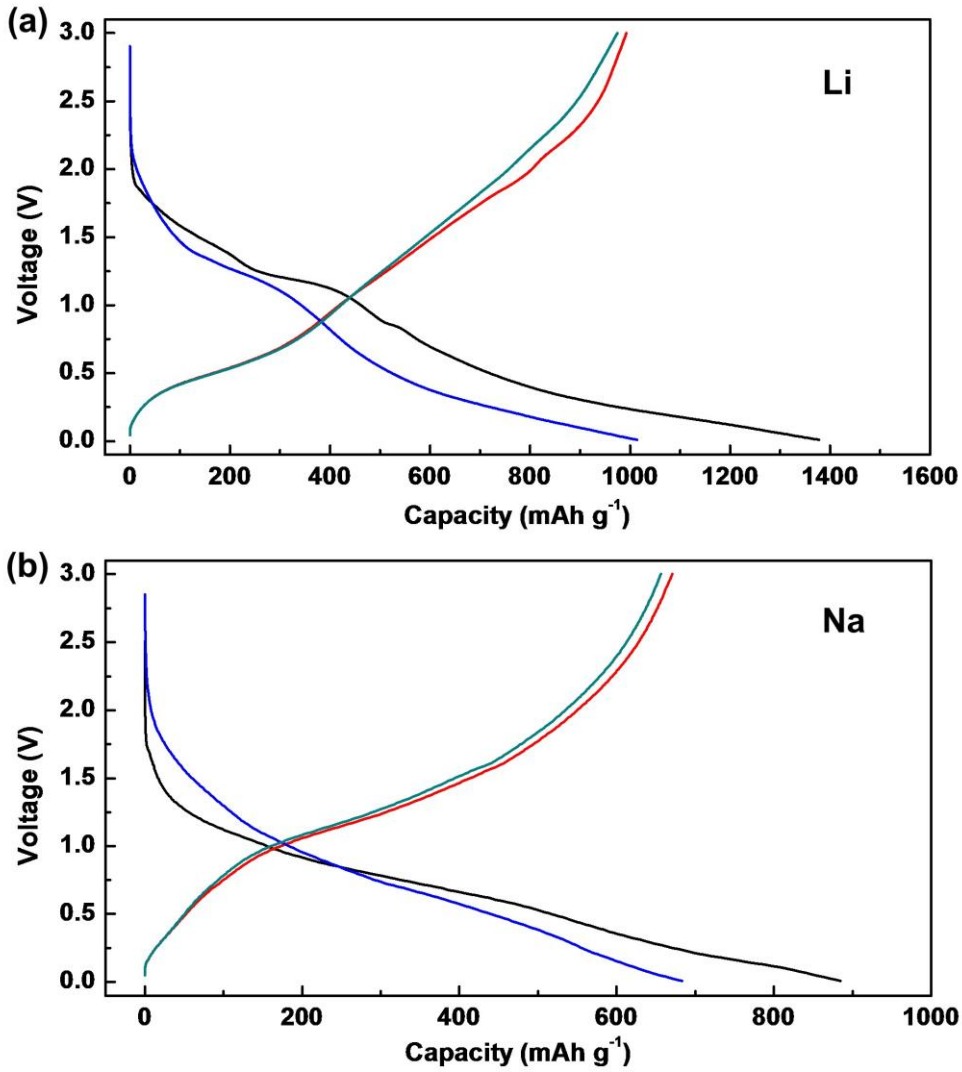

Fig. S13. Voltage profiles of the RGO/SnS_2@C for (a) LIBs and (b) NIBs cycled at a current density of 100 mA g^{-1} between 5mV and 3.0 V vs Li^+/Li and Na^+/Na, respectively.

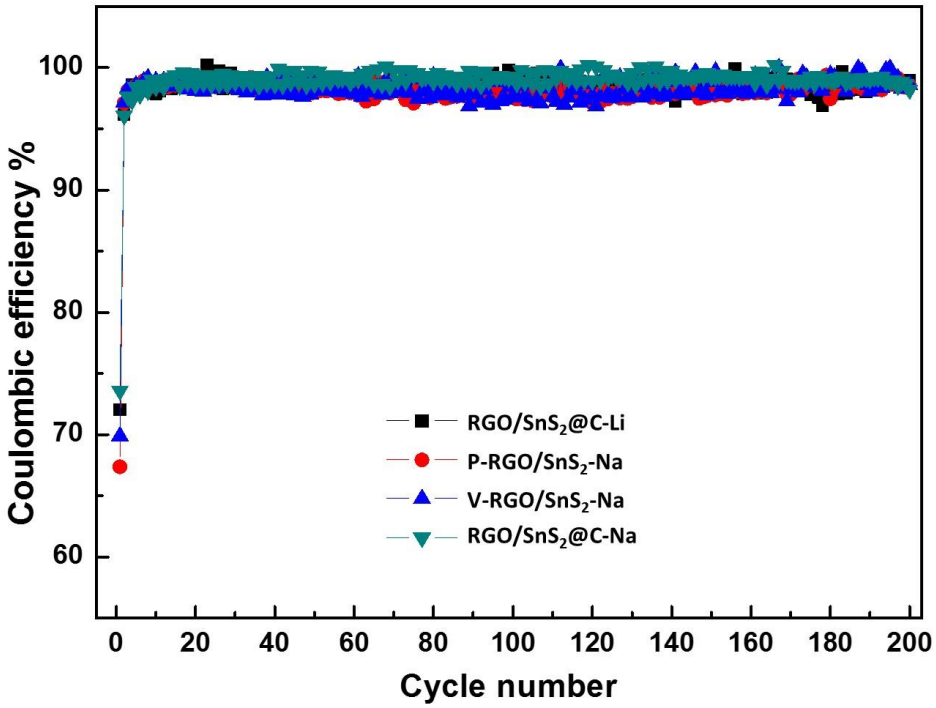

Fig. S14. Coulombic efficiency of P-RGO/SnS_2, V-RGO/SnS_2, and RGO/SnS_2@C for LIBs and/or NIBs cycled at a current density of 100 mA g^{-1} between 5mV and 3.0 V vs Li^+/Li and Na^+/Na, respectively.

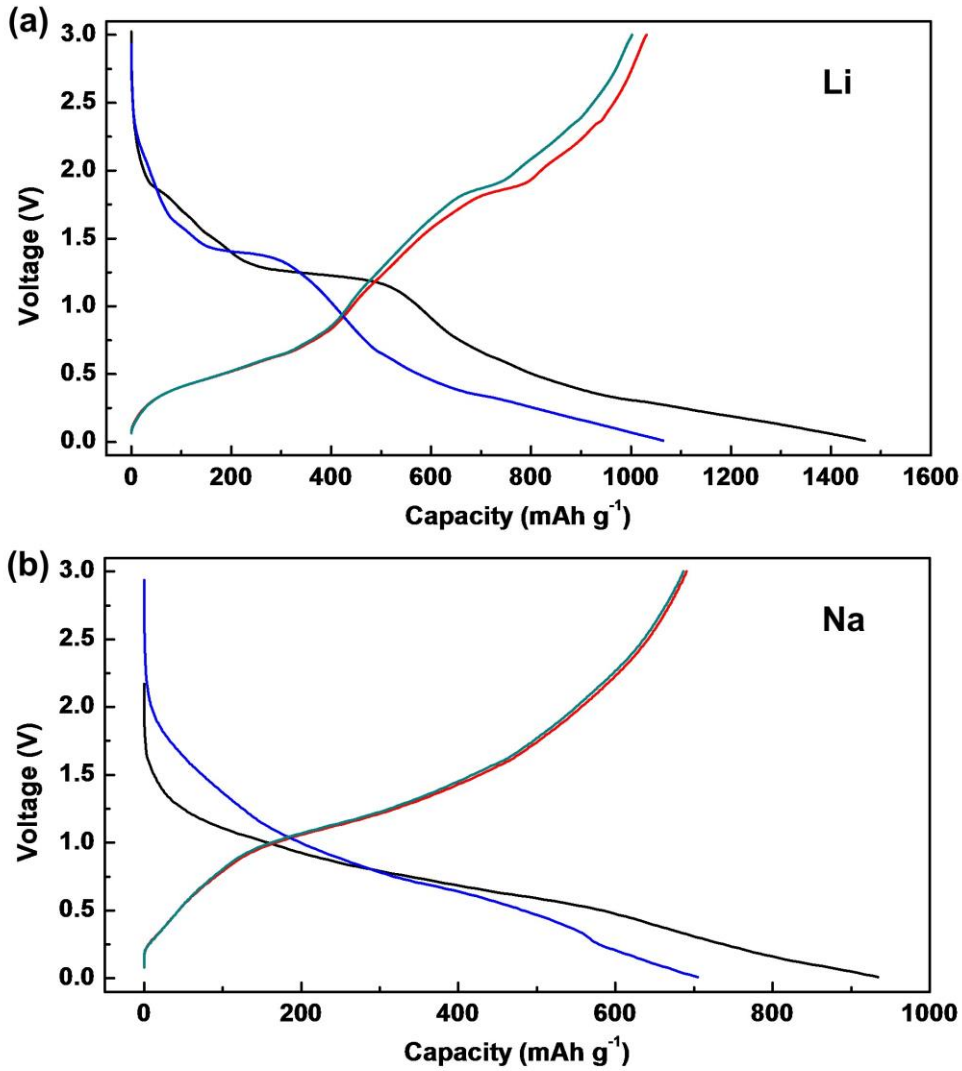

Fig. S15. Voltage profiles of the CNT/SnS_2@C for (a) LIBs and (b) NIBs cycled at a current density of 100 mA g^{-1} between 5mV and 3.0 V vs Li^+/Li and Na^+/Na, respectively.

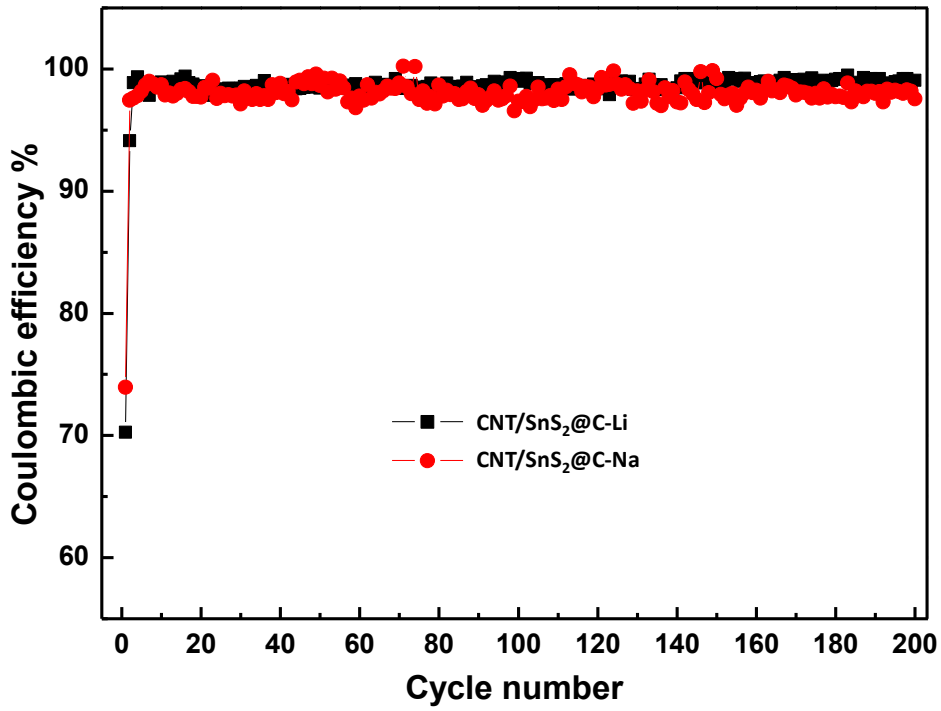

Fig. S16. Coulombic efficiency of the CNT/SnS_2@C for LIBs and NIBs cycled at a current density of 100 mA g^{-1} between 5mV and 3.0 V vs Li^+/Li and Na^+/Na, respectively.

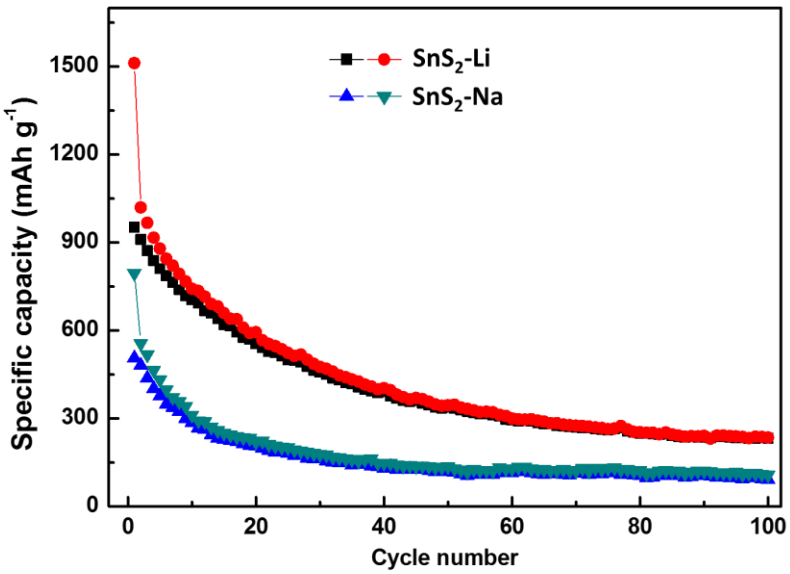

Fig. S17. Cycling performance of the as-synthesized bare SnS_2 for Li-ion and Na-ion storage at 100 mA/g.

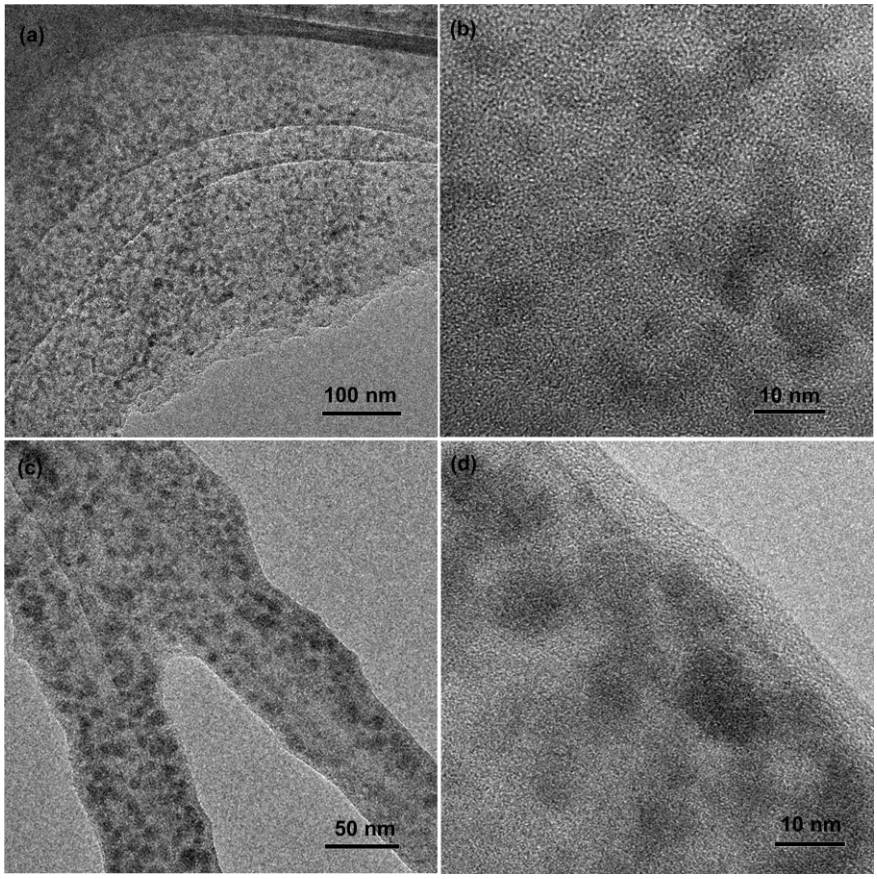

Fig. S18. TEM images of (a, b) RGO/SnS_2@C and (c, d) CNT/SnS_2@C electrodes for LIBs after 200 cycles.

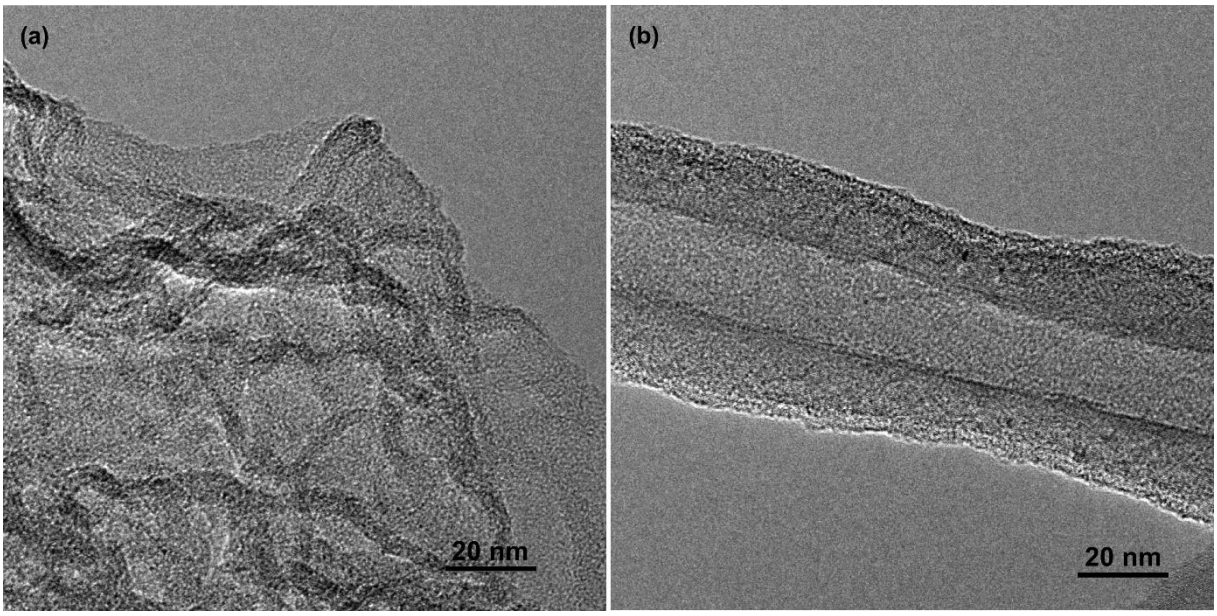

Fig. S19. TEM images of (a) the as-synthesized RGO/glucose-derived carbon (RGO@C) and (b) CNT/glucose-derived carbon (CNT@C) composites without SnS_2 phase.

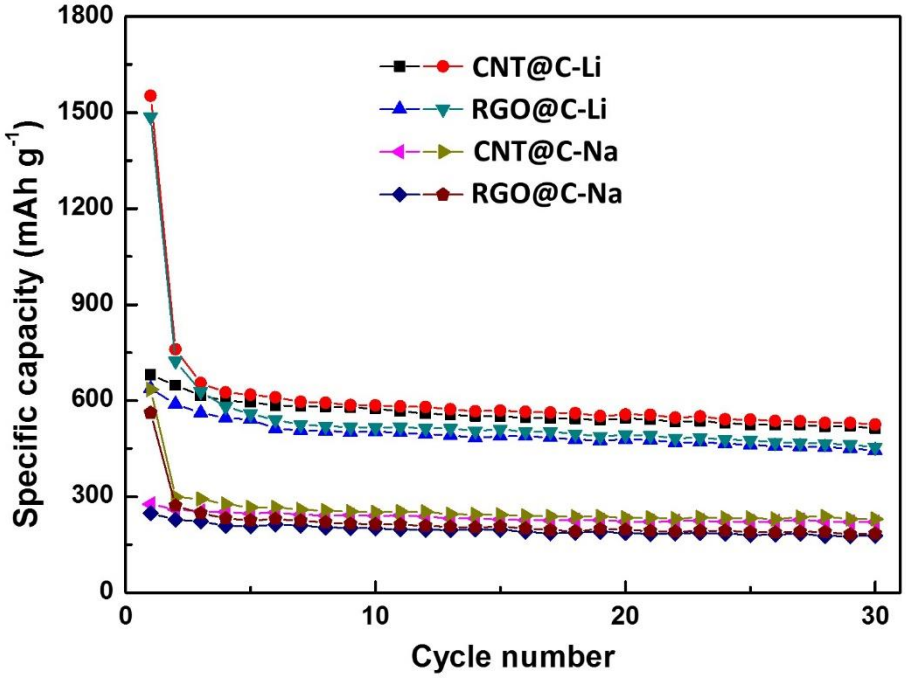

Fig. S20. Cycling performance of the as-synthesized RGO/glucose-derived carbon (RGO@C) and CNT/glucose-derived carbon (CNT@C) composites without SnS_2 phase at 100 mA/g.

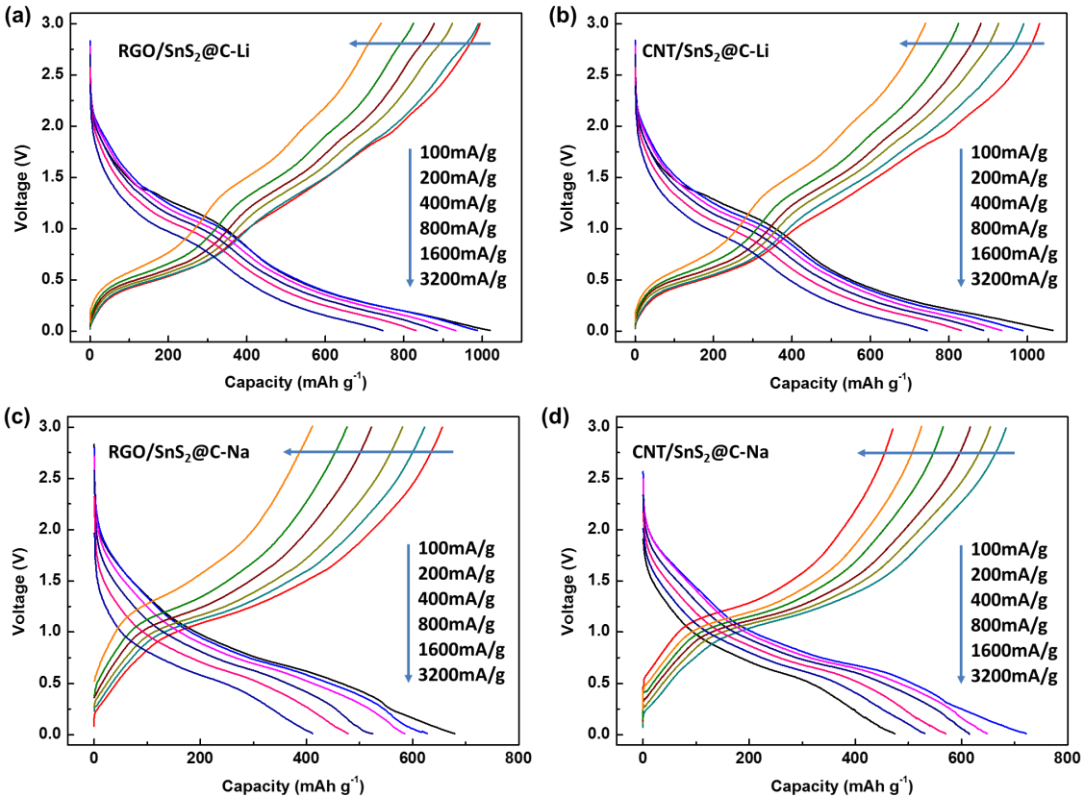

Fig. S21. Voltage profiles of the carbon coated composites for Li^+ or Na^+ storage at various current rates.

Table S3. Electrochemical performance comparison of some representative SnS_2/nanocarbons composite anodes for lithium/sodium ion batteries.

	Materials	Tin Sulphide content (wt. %)	Testing Voltage window (V)	Cycling Performance			Rate Capability	Ref.
				Current density (mA g^{-1})	Initial Capacity (mAh g^{-1})*	Capacity retention(mAh g^{-1})/ cycling number*	Capacity (mAh g^{-1}) @Current density (mA g^{-1}) *	
Li	Graphene/SnS_2	~95	0.01-1.3	50	687	650/30	230@6400	[1]
	SnS_2-RGO	~68.4	0.005-3.0	66	1077	896/40	934@660	[2]
	SnS_2/graphene hybrid	~70	0.005-3.0	800	864	704/100	546@6400	[3]
	SnS_2-RGO	~93.2	0.01-3.0	120	738	564/60	151@3000	[4]
	SnS_2 on 3D graphene	53.7	0.01-2.0	1000	451	~450/50	174@2000	[5]
	carbon-coated SnS_2	87	0.0-1.2	50	707	668/50	~590@1C	[6]
	SnS_2/SWCNT	34.9	0.01-3.0	1000	~700	509/100	498@2000	[7]
	RGO/SnS_2@C	86.2	0.005-3.0	100	992	908/200	656@3200	This work
	CNT/SnS_2@C	77.1	0.005-3.0	100	1031	940/200	741@3200	This work
Na	SnS_2 NC/EDA–RGO	75	0.01-3.0	200	749	680/100	250@11200	[8]
	SnS_2/C Nanospheres	41	0.005-2.5	50	660	600/100	360@1000	[9]
	2D SnS_2 nanosheets	100	0.005-3.0	100	733	647/50	435@2000	[10]
	SnS_2/rGO	81	0.005-3.0	800	469	400/1000	337@12800	[11]
	Layered SnS_2-RGO		0.01-2.5	200	630	628/100	544@2000	[12]
	SnS_2/graphene	65.5	0.005-3.0	20	725	670/60	463@640	[13]
	SnS_2-rGO Composite	88	0.01-2.5	200	630	627/100	-	[14]
	SnS_2/graphene		0.01-2.5	200	650	610/300	326@4000	[15]
	RGO/SnS_2@C	86.2	0.005-3.0	100	650	580/200	412@3200	This work
	CNT/SnS_2@C	77.1	0.005-3.0	100	691	605/200	462@3200	This work

*: The gravimetric capacity values are based on the active material including carbon and tin sulphide.

References

[1] B. Luo, Y. Fang, B. Wang, J. Zhou, H. Song, L. Zhi, *Energ Environ Sci* **2012**, 5, 5226.
[2] P. Chen, Y. Su, H. Liu, Y. Wang, *Acs Appl. Mater. Inter.* **2013**, 5, 12073.
[3] S. Y. Liu, X. Lu, J. Xie, G. S. Cao, T. J. Zhu, X. B. Zhao, *Acs Appl. Mater. Inter.* **2013**, 5, 1588.
[4] J. F. Yin, H. Q. Cao, Z. F. Zhou, J. X. Zhang, M. Z. Qu, *J. Mater. Chem.* **2012**, 22, 23963.
[5] H. Zhi Xiang, W. Ye, W. Jen It, Y. Hui Ying, *2D Mater.* **2015**, 2, 024010.
[6] H. S. Kim, Y. H. Chung, S. H. Kang, Y. E. Sung, *Electrochimica Acta* **2009**, 54, 3606.
[7] Y. Liu, C. Wang, H. Yang, Z.-J. Shi, F.-Q. Huang, *Mater. Lett.* **2015**, 159, 329.
[8] Y. Jiang, M. Wei, J. Feng, Y. Ma, S. Xiong, *Energ Environ Sci* **2016**.
[9] J. Wang, C. Luo, J. Mao, Y. Zhu, X. Fan, T. Gao, A. C. Mignerey, C. Wang, *Acs Appl. Mater. Inter.* **2015**, 7, 11476.
[10] W. Sun, X. Rui, D. Yang, Z. Sun, B. Li, W. Zhang, Y. Zong, S. Madhavi, S. Dou, Q. Yan, *ACS Nano* **2015**, 9, 11371.

[11] Y. Zhang, P. Zhu, L. Huang, J. Xie, S. Zhang, G. Cao, X. Zhao, *Adv. Funct. Mater.* **2014**, n/a.
[12] B. Qu, C. Ma, G. Ji, C. Xu, J. Xu, Y. S. Meng, T. Wang, J. Y. Lee, *Adv. Mater.* **2014**, 26, 3854.
[13] X. Xie, D. Su, S. Chen, J. Zhang, S. Dou, G. Wang, *Chemistry – An Asian Journal* **2014**, 9, 1611.
[14] C. Ma, J. Xu, J. Alvarado, B. Qu, J. Somerville, J. Y. Lee, Y. S. Meng, *Chem. Mater.***2015**, 27, 5633.
[15] Y. Liu, H. Kang, L. Jiao, C. Chen, K. Cao, Y. Wang, H. Yuan, *Nanoscale* **2015**, 7, 1325.